Nilsson parameters κ and μ in relativistic mean field models

A. Sulaksono,[1] T. Mart,[1] and C. Bahri[1,2]
[1]*Departemen Fisika, FMIPA, Universitas Indonesia, Depok 16424, Indonesia*
[2]*Department of Physics and Astronomy, Louisiana State University, Baton Rouge, Louisiana 70803, USA*
(Received 5 October 2004; published 22 March 2005)

Nilsson parameters κ and μ have been studied in the framework of relativistic mean field (RMF) models. They are used to investigate the reason why RMF models give a relatively good prediction of the spin-orbit splitting but fail to reproduce the placement of the states with different orbital angular momenta. Instead of the relatively small effective mass M^*, the independence of M^* from the angular momentum l is found to be the reason.

DOI: 10.1103/PhysRevC.71.034312 PACS number(s): 21.10.Pc, 21.60.Cs

I. INTRODUCTION

The finite-range (FR) (see Refs. [1–4] for a review) and point-coupling (PC) (see Refs. [5–7] for a review) types of relativistic mean field (RMF) models have been successful in describing the bulk properties as well as the deformation in a wide mass spectrum of nuclei. The interconnection of the models and their relations to nonrelativistic models, like the Skyrme-Hartree-Fock (SHF) ones, have been established [8]. The role of the exchange in RMF-FR [9–13] and RMF-PC [14] models for finite nuclei has also been explored.

Significant attention has been paid to exploring the role of the spin-orbit potential ($V_{L\text{-}S}$) in RMF models for various problems and applications connected to single-particle spectra predictions (see, for example, Refs. [2,13,15–21]). The standard parameter set of the Nilsson model has also been quite successful in reproducing single-particle spectra of stable nuclei [22]. New parameter sets were proposed to improve the predictability of the model for neutron-rich [23] and proton-rich [24] nuclei. Single-particle levels of these parameter sets are compared in Refs. [23,24] with those obtained by SHF and RMF models. We also note that the origin of the prolate dominance shapes over the oblate ones can be explained in the framework of a Nilsson model as an effect of the strong interference between spin-orbit and orbit-orbit terms of the Nilsson potential [25]. So far, however, except for the pseudo-spin symmetry study in finite nuclei [26], there have been no other investigations of the role of the orbit-orbit potential (V_{LL}) which is directly derived from RMF models.

Odd nuclei and single-particle spectra in an RMF-FR model using different levels of approximation (spherical and deformed) were computed and compared in Ref. [27]. In Ref. [13], single-particle splitting energies between spin-orbit partners along some isotonic chain (O, Ca, Sn) were also examined in the framework of RMF, SHF, and relativistic Hartree-Fock models. Furthermore, another method studies spin-orbit potential by exploring the high-spin data [28]. With this method one can avoid the scarce and uncertain data available on spin-orbit splittings and their isotopic as well as isotonic dependences. Here we quote from Ref. [28], for example, that the most recent experimental data evaluations [29] give $\Delta\epsilon_{d_{3/2}-d_{5/2}} \approx 6$ MeV for ^{40}Ca and $\Delta\epsilon_{d_{3/2}-d_{5/2}} \approx 5$ MeV for ^{48}Ca, while older works give $\Delta\epsilon_{d_{3/2}-d_{5/2}} \approx 6.8$ [30], 7.3 [31], and 7.7 [32] MeV for ^{40}Ca and $\Delta\epsilon_{d_{3/2}-d_{5/2}} \approx 5.3$ MeV [32] for ^{48}Ca. More detailed information on single-particle levels can be found in Ref. [33]. Since the method is based on a direct comparison of the excitation energies of terminating states, the correlations beyond the mean field can be strongly suppressed. Nevertheless, this method is still constrained by the limited knowledge of the time-odd component of the nonrelativistic mean field [28].

In this paper, we will revisit and study the single-particle spectra (SPS) of ^{208}Pb, ^{132} Sn, and ^{40}Ca in the RMF models in order to understand the origin of their predictive powers for spin-orbit splitting and the reason why the relative placements of the states with different orbital angular momenta l are not well reproduced [27]. Afterward, we will try to find the connection between their SPS predictions and their effective masses M^* through their $V_{L\text{-}S}$ and V_{LL} potentials in ^{208}Pb. Spherically symmetric calculations are used because of the robustness of the spectral differences against polarization effects [27].

We choose NL-Z, NL-Z2, NL-VT1 (RMF-FR) [2,15,34], and PC-F1 (RMF-PC) [7] because they have nearly the same procedure to adjust their coupling constants, hence the prediction bias due to the different fitting procedure can be minimized.

II. SPS PREDICTIONS OF RMF MODELS

In this section, we will study the ^{208}Pb, ^{132} Sn, and ^{40}Ca SPS predictions of RMF models. The experimental single-particle data are taken from [33]. The ^{208}Pb neutron ($2f_{7/2}$ and $1h_{9/2}$) and proton ($2d_{5/2}$ and $1g_{7/2}$) data as well as the ^{40}Ca neutron ($1d_{5/2}$) and proton ($1d_{5/2}$) data are obtained by averaging over the spectroscopic factors [33]. To analyze the relative position between two different levels with different angular momenta α we use the formulas [20]

$$\bar{E}_l = \sum_{j=l-1/2}^{j=l+1/2} \frac{(2j+1)E_j}{2(2l+1)},$$
$$\alpha_{lk} = \bar{E}_l - \bar{E}_k, \tag{1}$$

where $\bar{E}_l$ is the average energy of the spin-orbit partner with angular momentum l. The relative position between k and l levels α_{lk} can be determined from the difference between $\bar{E}_l$ and $\bar{E}_k$.

 ©2005 The American Physical Society

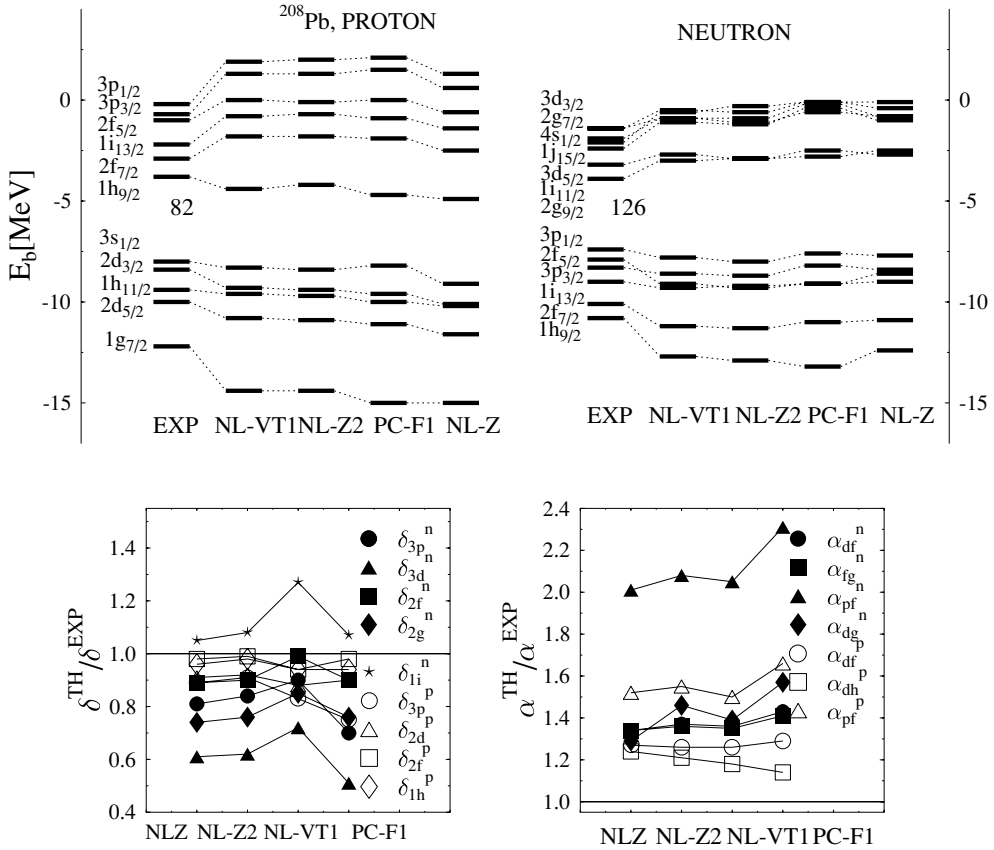

FIG. 1. Single-particle spectra (SPS) for ^{208}Pb (top): left and right panels are for a proton and neutron, respectively. Spin-orbit splitting δ and relative position between two different levels with different angular momenta α of ^{208}Pb are shown in the left- and right-bottom panels. Experimental data (EXP) are taken from Ref. [33]. RMF models with NL-Z, NL-Z2, NL-VT1, and PC-F1 parametrizations are shown.

Figure 1 shows the SPS for ^{208}Pb. In the top panels, it can be seen that all models have a similar trend in placing and ordering the proton and neutron single-particle energies. The gap between occupied and unoccupied levels is relatively well reproduced for the proton but quite poorly for the neutron case. Compared with experimental data, the SPS lines do not coincide. The deviations show up significantly in the $1g_{7/2}$, $3p_{3/2}$, and $3p_{1/2}$ proton states and in the $1h_{9/2}$ neutron state. For the neutron spectrum, similar to Ref. [27], the ordering is reversed among the $1i_{13/2}$, $3p_{3/2}$, and $2f_{5/2}$ states. There are quite significant discrepancies in the spacing between the $1i_{11/2}$ and $3d_{5/2}$ states, as well as between the $1h_{9/2}$ and $2f_{7/2}$ states, with experimental data. For the proton spectrum, discrepancies occur between the $1h_{9/2}$ and $2f_{7/2}$ states and between the $2d_{5/2}$ and $2g_{7/2}$ states.

The trends of the spin-orbit splitting (see the lower-left panel of Fig. 1) and the relative position of SPS (lower-right panel of Fig. 1) of NL-Z are similar to those of NL-Z2 but different from those of NL-VT1 and PC-F1. For the proton, except for the splitting in $3p$ states of PC-F1, all parameter sets have only 15% deviation from their experimental values. Nevertheless, since the positions of $3p$ states are quite far from the Fermi surface, we can say that all parameter sets give a good prediction of the proton spin-orbit splitting. In the case of the neutron, only the splitting of $2f$ states deviates by less than 10% from the experimental value. NL-VT1 has four gaps with deviations in splitting less than 20%. Unfortunately, it has a gap ($1i$ states) with a more than 20% deviation, and the gap is larger than the corresponding experimental data. The position of these states is above the Fermi surface. NL-Z2 and NL-Z have more or less 20% deviation in the splitting of $3p$ states (the position of these states is around the Fermi surface), and for PC-F1 the deviation of that splitting is larger than 20%. A quite large deviation appears in the splitting of $3d$ and $2g$ states (the positions of both spin-orbit partners are above the Fermi surface). It seems that all parameter sets are unable to give good predictions in the neutron spin-orbit splitting. The SPS relative position of the proton has a better prediction than that of the neutron. The proton has two α values with deviations less than 30% and one α above the Fermi level (α_{pf}). We also note that α_{pf} has 60% deviation. The neutron has three α with deviations from experimental data between 30% and 50%, and it has even one α (α_{pf}) that deviates by about 100% from experimental data. The positions of those states ($3p$ and $2f$) are around the Fermi surface.

Figure 2 shows the SPS for ^{132}Sn. In the top panels, all models have similar trends in level placing and ordering. Their SPS lines do not coincide with experimental data. For the neutron spectrum, the reversed ordering between $2d_{3/2}$ and the $3s_{1/2}$ and $2h_{11/2}$ states occurs. A significant difference in

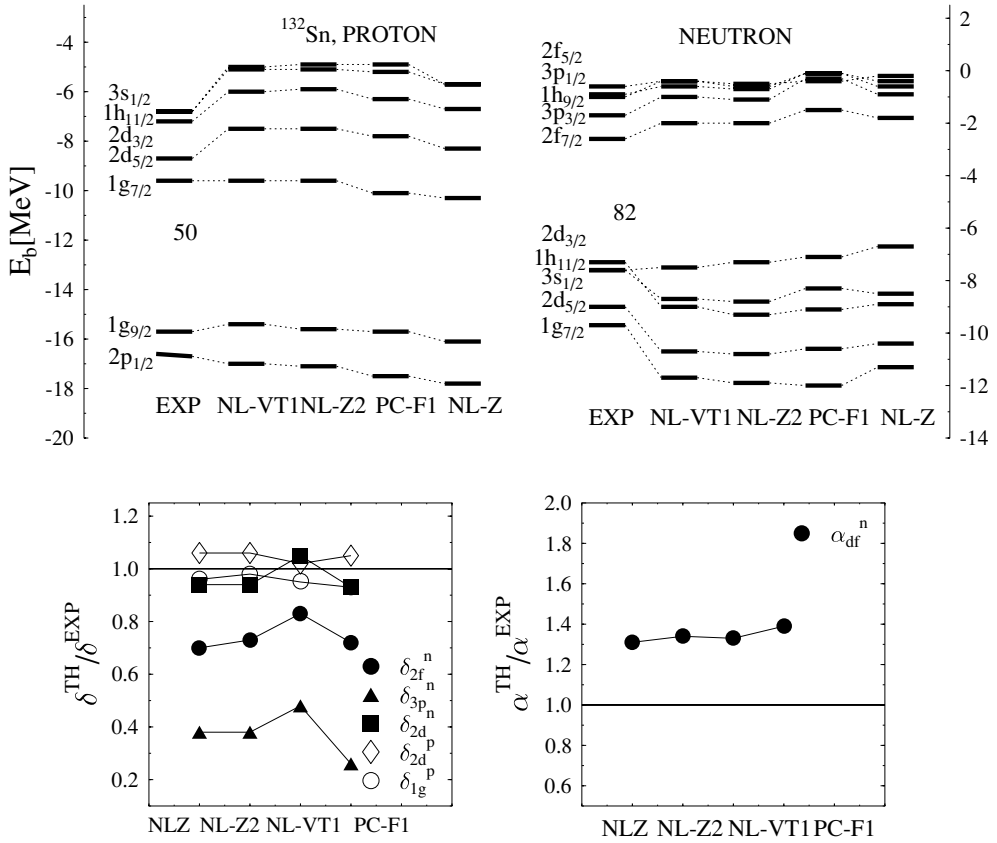

FIG. 2. Same as Fig. 1, but for ^{132}Sn.

spacing with experimental data occurs between the $2d_{5/2}$ and $1g_{7/2}$ states of the proton. The bottom panels show that all parameter sets predict acceptable spin-orbit splittings for the proton but not for the neutron. The relative position between $2d$ and $2f$ levels for neutron (α^n_{df}) deviates by almost 40% from experimental data. The trends of the spin-orbit splitting (see the lower-left panel of Fig. 2) and the relative position of the SPS (lower-right panel) of NL-Z are similar to those of NL-Z2 but different from those of NL-VT1 and PC-F1.

Figure 3 shows the SPS for ^{40}Ca. The upper-left panel (proton) shows that NL-VT1 reproduces experimental values of every single-particle energy. PC-F1 has a too narrow spacing between the $1d_{3/2}$ and $2s_{1/2}$ states. The reversed ordering of the $2f_{5/2}$ and $2p_{1/2}$ states occurs in the case of NL-Z and NL-Z2. In the upper-right panel (neutron), the models do not really have a similar trend in level placing and ordering. Similar to the case of the proton, PC-F1 again has a too narrow spacing between the $1d_{3/2}$ and $2s_{1/2}$ states. The lower panels show that in contrast to ^{208}Pb and ^{132}Sn, ^{40}Ca has a better spin-orbit splitting for the neutron rather than for the proton. The relative positions between $1d$ and $1f$ levels for the neutron and proton (α^n_{df}) deviate by less than 20% from experimental data.

These results confirm the findings of Ref. [27] that the relative placement and ordering of the states in RMF models are not well reproduced. In addition, we note that RMF-FR (NL-Z, NL-Z2, and NL-VT1) has a better prediction than RMF-PC (PC-F1), and the presence of the tensor terms (NL-VT1) enhances the improvements in placing and ordering of single-particle states, particularly in lighter nuclei (e.g., ^{40}Ca). However, these improvements are still not adequate to overcome the problem.

III. NILSSON PARAMETERS κ AND μ OF RMF MODELS

It has been known that all models presented here have $M^*/m \approx 0.6$. Unlike the non-self-consistent calculations (models using Wood-Saxon or Nilsson potentials), where the SPS has a direct connection with the potential parameters, the connection is not so obvious in the RMF models because it is hidden by the self-consistency condition. Therefore, it is natural to translate M^*/m of RMF models into V_c, V_{LL}, and $V_{L\text{-}S}$ by taking a nonrelativistic limit, where they resemble a Wood-Saxon or Nilsson potential. The interpretation of the results of this section will be given in the next section by varying M^*/m in one model and studying its SPS prediction for ^{208}Pb.

The Hamiltonian of the RMF model in spherical systems is

$$H = \vec{\alpha} \cdot (\vec{p} + i\gamma_0 \vec{T}) + \gamma_0(m + S) + V_0, \tag{2}$$

where $H\Psi^{\pm}_k = \epsilon^{\pm}_k \Psi^{\pm}_k$ is fulfilled. Using the general convention for Ψ^+_k, i.e.,

$$\Psi^+_k = \begin{pmatrix} g_k \chi_k^{m_j} \\ i f_k \chi_{-k}^{m_j} \end{pmatrix},$$

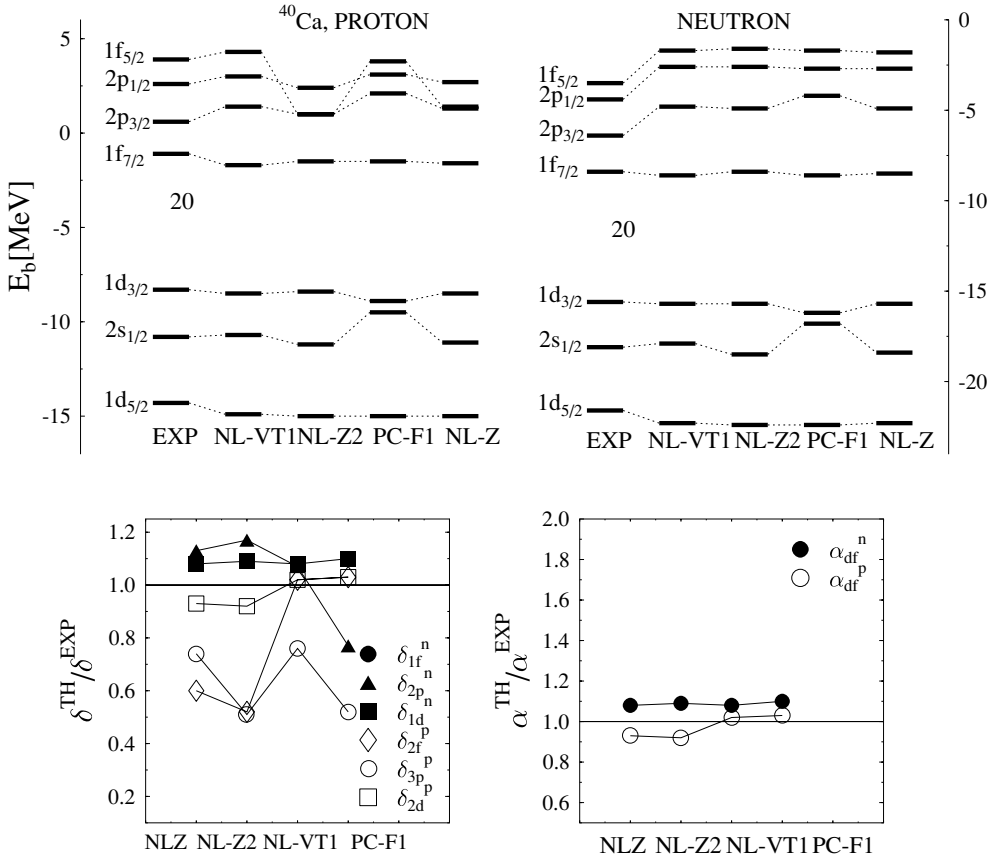

FIG. 3. Same as Fig. 1, but for ^{40}Ca.

the positive energy equation for the upper component becomes

$$\left[\partial_r^2+\frac{2}{r}\partial_r-\frac{\vec{L}^2}{r^2}-\left(\frac{(\partial_r\Delta)}{\left(2m+\epsilon_k^{+\prime}-\Delta\right)}-2T_r\right)\frac{\vec{\sigma}\cdot\vec{L}}{r}+\frac{(\partial_r\Delta)}{\left(2m+\epsilon_k^{+\prime}-\Delta\right)}\partial_r+\left(\frac{2T_r}{r}-T_r^2+(\partial_r T_r)+\frac{(T_r\partial_r\Delta)}{\left(2m+\epsilon_k^{+\prime}-\Delta\right)}\right)+\left(\epsilon_k^{+\prime}-\Sigma\right)\left(2m+\epsilon_k^{+\prime}-\Delta\right)\right]g_k=0, \tag{3}$$

with $\Sigma=S+V_0$, $\Delta=V_0-S$, and $\epsilon_k^{+\prime}=\epsilon_k^{+}-m$, while S, V_0, and $\vec{T}$ indicate the scalar, time-component of the vector, and tensor potentials, respectively. The nonrelativistic form of Eq. (3) can be derived. The Darwin term $(\frac{(\partial_r\Delta)}{(2m+\epsilon_k^{+\prime}-\Delta)}\partial_r)$ in Eq. (3) can be absorbed by transforming the g_k wave function into a new one, G_k^+ [16]. This leads to a Schrödinger form, i.e.,

$$\left(\frac{p_r^2}{2m}+\frac{\boldsymbol{L^2}}{2mr^2}+V_c(r,\epsilon^{+\prime})+V_{L\text{-}S}(r,\epsilon^{+\prime})\frac{\boldsymbol{\sigma}\cdot\boldsymbol{L}}{r}\right)G_k^+=\epsilon^{NR}G_k^+, \tag{4}$$

where $\epsilon^{NR}=\epsilon^{+\prime}(1+\frac{\epsilon^{+\prime}}{2m})$ [16]. In finite nuclei, the second term in ϵ^{NR} is smaller than 1, and

$$V_{L\text{-}S}(r,\epsilon^{+\prime})=\frac{1}{2m}\left[\frac{(\partial_r\Delta)}{(2m+\epsilon^{+\prime}-\Delta)}-2T_r\right], \tag{5}$$

$$V_c(r,\epsilon^{+\prime})=\Sigma-\frac{\Sigma\Delta}{2m}+\frac{(\Sigma+\Delta)\epsilon^{+\prime}}{2m}+\frac{3}{8}\frac{(\partial_r\Delta)^2}{m(2m+\epsilon^{+\prime}-\Delta)^2}+\frac{1}{2}\frac{(\partial_r\Delta)}{m(2m+\epsilon^{+\prime}-\Delta)r}+\frac{1}{4}\frac{\left(\partial_r^2\Delta\right)}{m(2m+\epsilon^{+\prime}-\Delta)}+\frac{1}{2m}\left[\frac{-2T_r}{r}+T_r^2-\partial_r T_r-\frac{(T_r\partial_r\Delta)}{(2m+\epsilon^{+\prime}-\Delta)}\right]. \tag{6}$$

In heavy nuclei, the mean field central potential V_c and the spin-orbit potential $V_{L\text{-}S}$ are closer to the nonrelativistic results obtained by using the Wood-Saxon potential [35]. Unlike the Wood-Saxon results, the RMF model has a strong energy-dependent V_c and a weak energy-dependent $V_{L\text{-}S}$ (Fig. 4). In ^{208}Pb, V_c^n is deeper than V_c^p because more neutrons are present than protons. $V_{L\text{-}S}$ of the RMF model (NL-VT1) is deeper than the Wood-Saxon prediction [35]. The tensor term gives only a minor additional contribution to spin-orbit potential near the Fermi surface. There is no significant difference between the neutron and proton $V_{L\text{-}S}$ of ^{208}Pb in the RMF model (NL-VT1).

The study of nonrelativistic potentials of RMF models has been done in many places with different intentions and different methods to obtain V_c and $V_{L\text{-}S}$ [2,13,15–20].

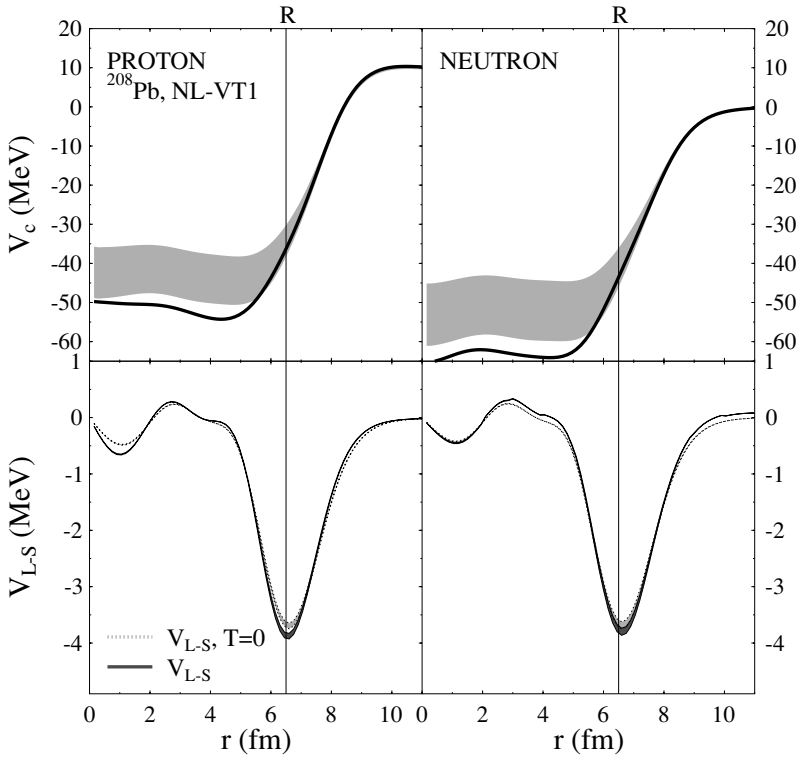

FIG. 4. Shaded areas are the energy-dependent central potential V_c (top) and the spin-orbit potential $V_{L\text{-}S}$ (bottom). The proton and neutron parts are shown in the left and right panels, respectively. $R = 1.1\,A^{1/3}$ fm is the Fermi surface radius. Solid lines in the top are obtained from the summation of the scalar and time components of vector potentials (the dominant term in V_c). NL-VT1 parametrization is used. $T = 0$ (bottom) means that the tensor potential is turned off.

However, a nonrelativistic form of the RMF model like the Nilsson has not yet been explored, especially in analyzing the SPS. The advantage of using the Nilsson model is that V_{LL} could be employed to analyze the relation between states of different l and their orderings. Reference [26] calculates V_{LS} and V_{LL} from several RMF models by using some different approximations to study the origin of the pseudo-spin symmetry. We note that the maximum value of $\epsilon^{+\prime}$ has the same order of magnitude as the difference value between the scalar and time components of vector potentials (Σ); e.g., in the ^{208}Pb neutron, the corresponding value is around 50 MeV. On the other hand, Δ is a summation of the scalar and time components of the vector potential, and the corresponding maximum value for the ^{208}Pb neutron is more or less 400 MeV. It is also known that the nucleon mass is around 1000 MeV [2]. Therefore, to obtain a "Nilsson form" we can assume that $\epsilon^{+\prime} < \Delta < m$, so that $\epsilon^{NR} = \epsilon^{+\prime}(1 + \frac{\epsilon^{+\prime}}{2m}) \approx \epsilon^{+\prime}$ and $(2m + \epsilon^{+\prime} - \Delta)^{-1} \approx (2m - \Delta)^{-1}$. After that, Eq. (4) can be written as

$$\left(\frac{p_r^2}{2m} + \frac{L^2}{2mr^2} + V_c^{\text{eff}}(r) + V_{LL}^{\text{eff}}(r)\boldsymbol{L}^2 + V_{L\text{-}S}^{\text{eff}}(r)s\cdot\boldsymbol{L}\right)G_k^+ \approx \epsilon^{+\prime}G_k^+, \tag{7}$$

where $s = \frac{1}{2}\boldsymbol{\sigma}$ and

$$V_c^{\text{eff}}(r) = \left[1 + \frac{\Sigma + \Delta}{\{2m - (\Sigma + \Delta)\}}\right]\lim_{\epsilon^{+\prime}\to 0} V_c(r, \epsilon^{+\prime}) - \frac{1}{2m}\left[\frac{(\Sigma + \Delta)}{\{2m - (\Sigma + \Delta)\}}\right]p_r^2,$$

$$V_{LL}^{\text{eff}}(r) = \frac{1}{2mr^2}\left[\frac{(\Sigma + \Delta)}{\{2m - (\Sigma + \Delta)\}}\right],$$

$$V_{L\text{-}S}^{\text{eff}}(r) = 2\left[1 + \frac{\Sigma + \Delta}{\{2m - (\Sigma + \Delta)\}}\right]\lim_{\epsilon^{+\prime}\to 0}\frac{V_{L\text{-}S}(r, \epsilon^{+\prime})}{r}. \tag{8}$$

As another consequence, the energy-dependent V_c transforms into energy-independent V_c plus a small nonlocal term (p_r dependent). Equation (7) can be considered as the Nilsson form of the RMF model. Both potentials can be compared with their partners from the Nilsson model through Nilsson parameters κ and μ [36].

The dominant parts of V_c^{eff} and $V_{L\text{-}S}^{\text{eff}}$ are taken merely to compare the predictions among the presented models (parameter sets). They have similar V_c^{eff} and $V_{L\text{-}S}^{\text{eff}}$ predictions not only for the proton but also for the neutron, especially near the Fermi surface. Small differences appear in the region around the center of nuclei, and a small V_c^{eff} deviation also appears in the unoccupied region of PC-F1. Thus, the forms of V_c^{eff} and $V_{L\text{-}S}^{\text{eff}}$ are essentially almost model independent (see Fig. 5).

In the Fermi surface, all parameter sets have similar κ and μ for the proton and neutron. On the contrary, the Nilsson model has different μ for proton and neutron (see Fig. 6). Compared with the Nilsson model (shaded regions), RMF ones have larger κ but smaller μ. The differences among all parameter sets (models) in κ appear only in the region close to the center of nuclei. It means that κ and μ of RMF models can be considered as model (parameter set) independent. Unlike in the Nilsson model, where κ and μ are independent of the position r, in RMF models both quantities

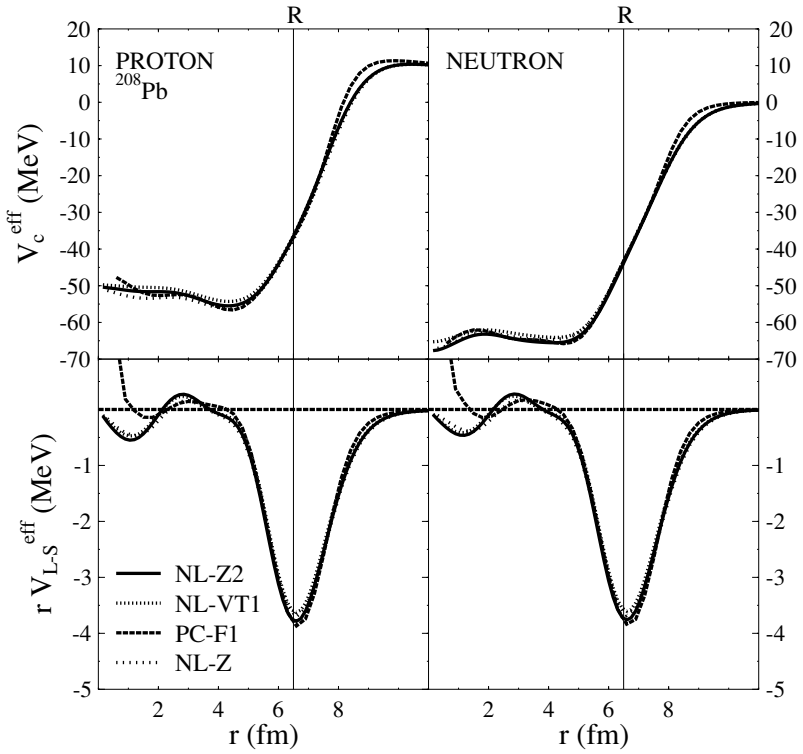

FIG. 5. Dominant part of the effective central potential $V_c^{\rm eff}$ (top) and spin-orbit potential $r V_{L\text{-}S}^{\rm eff}$ (bottom). Proton and neutron parts are shown in left and right panels, respectively. $R = 1.1\, A^{1/3}$ fm is the Fermi surface radius. Here, RMF models with NL-Z, NL-Z2, NL-VT1, and PC-F1 parametrizations are employed.

depend on r. The spatial dependence of $V_{L\text{-}S}^{\rm eff}$ originates mainly from the energy-dependent potential V_c. It should be noted that the nonrelativistic model, like SHF, does not have such dependence. Therefore, we can consider this spatial dependence as a genuine feature of self-consistent RMF models.

IV. INTERPRETATION

We prepared two variations of parameter sets to properly interpret the results. First, we varied the scalar coupling constant g_s of NL-Z until we obtained the desired M^*/m,

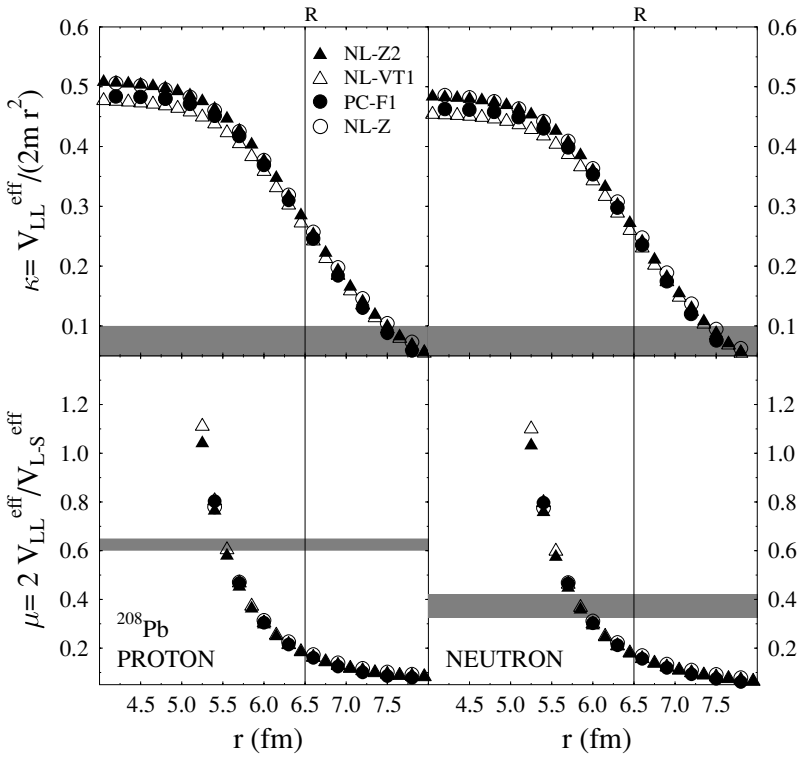

FIG. 6. Nilsson parameters κ (top) and μ (bottom) near the Fermi surface R. Left and right panels are for proton and neutron, respectively.

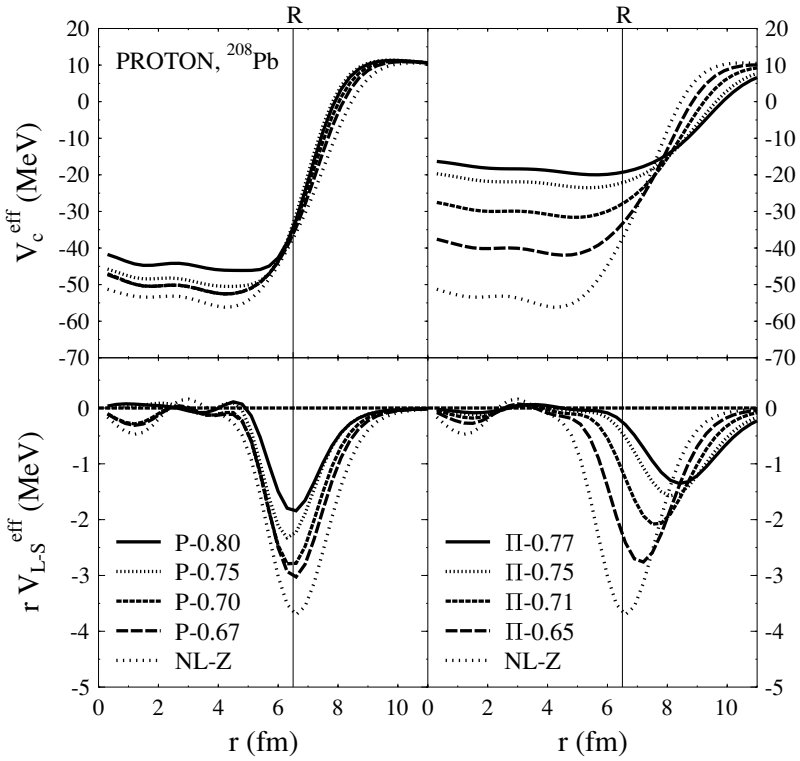

FIG. 7. Same as in Fig. 5, but parameter sets are adjusted with respect to certain M^*. P-067, P-0.70, P-0.75, and P-0.80 are fitted parameter sets. The fitting procedure is the same as in the case of NL-Z. Π-0.65, Π-0.70, Π-0.75, and Π-0.77 are unfitted parameter sets (obtained only by adjusting the value of coupling constant g_s).

while the four parameter sets were kept constant. Second, we fitted the four parameter sets with varied M^*/m. The parameter sets in the second procedure were obtained by fitting the four parameter sets into the same observable used in obtaining the NL-Z parameter set until they could reproduce nuclear matter properties. As in Ref. [2], the χ^2 became worse when M^*/m was larger than 0.6. The fitted parameter sets are tabulated in Table I, whereas their nuclear matter properties can be seen in Table II.

For the unfitted parameter sets (see the top-right panel of Fig. 7), the depth of $V_c^{\rm eff}$ and its trend around the Fermi surface drastically change. On the other hand, for the fitted parameter sets (top-left panel, Fig. 7), the depth and trend around the Fermi surface do not significantly change when M^*/m is varied. It means that the nuclear observable requires a cancellation between scalar and vector potentials. The scalar and vector potentials tend to weaken if M^*/m becomes larger than 0.6, but the $V_{L\text{-}S}^{\rm eff}$ is sensitive to the variation of M^*/m (lower panels, Fig. 7). $V_{L\text{-}S}^{\rm eff}$ decreases when M^*/m increases. The weakening of $V_{L\text{-}S}^{\rm eff}$ is due to the smallness of the spin-orbit splitting (upper-left panel, Fig. 9). Fitting the parameters to the nuclear observable does not help in this case. Therefore, only appropriate values of scalar and vector potentials can yield a correct $V_c^{\rm eff}$ and $V_{L\text{-}S}^{\rm eff}$ simultaneously. These potentials correspond to an M^*/m of about 0.6.

As can be seen in Fig. 8, the Nilsson parameter κ depends on M^*/m. The value of κ at the Fermi surface decreases when M^*/m increases, and the major effects are found for the fitted parameter sets. For these parameter sets, if $M^* = 0.77m$, it coincides with the prediction from the Nilsson model (shaded area). On the other hand, μ from the fitted parameter sets is almost independent of the M^*/m variation, while μ of the unfitted parameter sets depends on M^*/m. For the RMF models, therefore, a constant value of μ is the requirement for the correct nuclear bulk properties. The value

TABLE I. Numerical values of coupling constants used in the parameter sets. Except for the NL-Z parametrization [34], these values are adjusted with respect to M^*/m.

Parameter	NL-Z	P-0.67	P-0.70	P-0.75	P-0.80
g_S	10.06	8.91	8.45	7.58	7.22
g_V	12.91	11.02	10.26	8.73	7.94
g_R	9.69	9.69	9.69	9.69	9.69
b_2	−13.51	−13.44	−13.41	−13.06	−13.49
b_3	−40.22	−29.74	−24.48	−3.69	30.07
m_S	488.67	488.67	488.67	488.67	488.67
m_V	780	780	780	780	780
m_R	763	763	763	763	763

TABLE II. Nuclear matter properties predicted by NL-Z, P-067, P-0.70, P-0.75, and P-0.80 parametrizations.

Parameter	NL-Z	P-0.67	P-0.70	P-0.75	P-0.80
E/A (MeV)	−16.18	−16.30	−16.38	−16.34	−15.85
ρ_{nm} (fm^{-3})	0.15	0.16	0.16	0.17	0.16
M^*/m	0.58	0.67	0.70	0.75	0.80
a_4 (MeV)	41.7	41.1	42.0	42.8	39.7

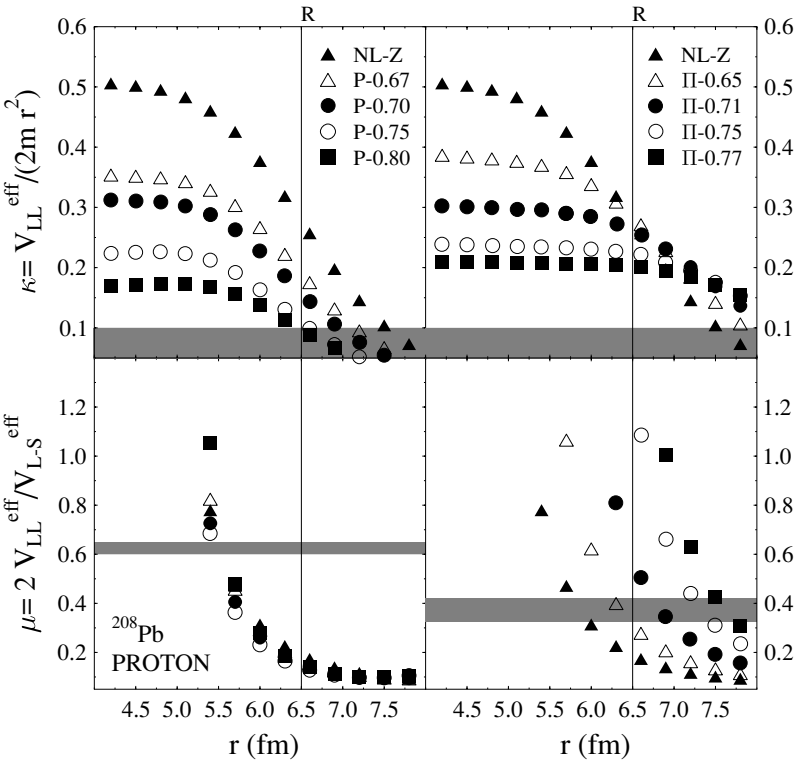

FIG. 8. Same as in Fig. 6, but using the P-067, P-0.70, P-0.75, P-0.80, Π-0.65, Π-0.70, Π-0.75, and Π-0.77 parameter sets.

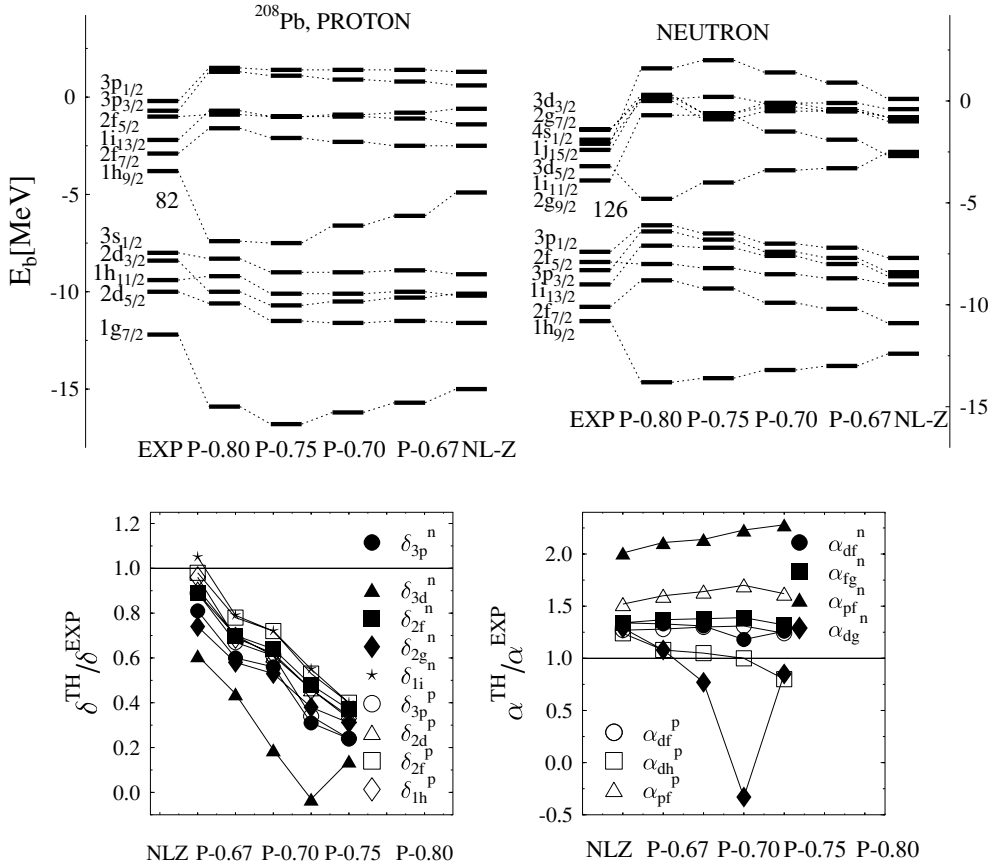

FIG. 9. Same as in Fig. 1, but using the P-067, P-0.70, P-0.75, and P-0.80 parameter sets.

of μ of the RMF models around the Fermi surface is smaller than that of the Nilsson model. In the RMF models, κ and μ depend on each other. As M^*/m increases, κ decreases and the spin-orbit potential becomes smaller in order to keep μ constant.

The variation of the neutron and proton SPS with respect to the variation of M^*/m is shown in Fig. 9. Some states are shifted up and others are shifted down as M^*/m increases. This combination does not improve the SPS relative position. The reason is mainly that the spin-orbit splitting becomes narrower when M^*/m increases. In the relative position between two different spin-orbit partners α, a couple of states are closer to experimental data, but the majority of states deviate more when M^*/m increases. The value of α_{dg} is negative for P-070 because there is an exchange of ordering in $3d$ states (the value of the gap is negative). Except for α_{dg}, all α values change quite drastically. This effect depends on M^*/m, but the pattern of changing is not the same for every level. It seems that the relative position α can be reproduced if M^*/m depends on the states. This dependence can be generated only if we take into account the exchange and/or other correlations (effects) beyond mean fields. It would be interesting to see whether the exchange effect can remedy this problem. Future calculations should address this question.

V. CONCLUSION

The ^{208}Pb, ^{132} Sn, and ^{40}Ca SPS of RMF models have been revisited and studied. Qualitatively, all RMF models presented here have a similar trend in SPS. Quantitatively, however, the SPS trends are different for each model. The comparison with new experimental data [33] shows not only that the position of the state is poorly reproduced, but also that some level positions in the neutron spectra are reversed.

The nonrelativistic limit of the RMF model has been derived in which the potentials resemble Wood-Saxon and Nilsson forms. The energy-dependent potentials V_c and V_{LS} (in Wood-Saxon type) of RMF models can be transformed into energy-independent potentials V_c^{eff} and V_{LS}^{eff} (in Nilsson type) but with an additional angular-momentum-dependent potential $V_{LL}^{\text{eff}}\boldsymbol{L}^2$. These potentials are used to analyze the ^{208}Pb SPS predictions from several RMF models. First we found that the behavior of κ and μ of the RMF models is different from that of the Nilsson model. Second, due to the interdependence of parameters κ and μ in the RMF models, the acceptable parameter sets ($M^*/m \approx 0.6$) at the Fermi surface need a relatively large V_{LL}^{eff} in order to maintain a correct spin-orbit splitting.

Since the effect of tensor terms in the RMF model is too small in the V_{LS} of heavy nuclei (^{208}Pb), the effect is marginal on giving correct level spacings and placement ordering. The suspicion that a relatively small V_{LL}^{eff} (large M^*/m) yields a relatively better placement of states is found to be wrong. The ^{208}Pb case demonstrated that when V_{LL}^{eff} is decreasing, only two placements of the states are improving, whereas the rest are getting worse. Therefore, the problem of RMF models in reproducing experimental data on the relative placement of the states seems to originate in the independence of M^* from l (state).

ACKNOWLEDGMENTS

A. S. acknowledges J. A. Maruhn and T. Cornelius for helpful comments in the early stage of this work.

[1] B. D. Serot and J. D. Walecka, Adv. Nucl. Phys. **16**, 1 (1986).
[2] P.-G. Reinhard, Rep. Prog. Phys. **52**, 439 (1989).
[3] B. D. Serot, Rep. Prog. Phys. **55**, 1855 (1992).
[4] P. Ring, Prog. Part. Nucl. Phys. **37**, 193 (1996).
[5] B. A. Nikolaus, T. Hoch, and D. G. Madland, Phys. Rev. C **46**, 1757 (1992).
[6] J. J. Rusnak and R. J. Furnstahl, Nucl. Phys. **A627**, 95 (1997).
[7] T. Buervenich, D. G. Madland, J. A. Maruhn, and P.-G. Reinhard, Phys. Rev. C **65**, 044308 (2002).
[8] A. Sulaksono, T. Buervenich, J. A. Maruhn, P.-G. Reinhard, and W. Greiner, Ann. Phys. (NY) **308**, 354 (2003).
[9] A. Bouyssy, J. F. Mathiot, N. V. Giai, and S. Marcos, Phys. Rev. C **36**, 380 (1987).
[10] H. F. Boersma and R. Malfliet, Phys. Rev. C **49**, 233 (1994); **49**, 1495 (1994).
[11] J. K. Zhang, Y. Jin, and D. S. Onley, Phys. Rev. C **48**, 2697 (1993).
[12] R. N. Schmid, E. Engel, and R. M. Dreizler, Phys. Rev. C **52**, 164 (1995); **52**, 2804 (1995); Found. Phys. **27**, 257 (1997).
[13] M. Lopez-Quelle, N. Van Giai, S. Marcos, and L. N. Savushkin, Phys. Rev. C **61**, 064321 (2000).
[14] A. Sulaksono, T. Buervenich, J. A. Maruhn, P.-G. Reinhard, and W. Greiner, Ann. Phys. (NY) **306**, 36 (2003).
[15] M. Bender, K. Rutz, P.-G. Reinhard, J. A. Maruhn, and W. Greiner, Phys. Rev. C **60**, 34304 (1999).
[16] M. Jaminon, C. Mahaux, and P. Rochus, Phys. Rev. C **22**, 2027 (1980).
[17] W. Koepf and P. Ring, Z. Phys. A **339**, 81 (1991).
[18] A. Baran, Phys. Rev. C **61**, 024316 (2000).
[19] R. J. Furnstahl, J. J. Rusnak, and B. D. Serot, Nucl. Phys. **A632**, 607 (1998).
[20] S. Yoshida and H. Sagawa, Nucl. Phys. **A658**, 3 (1999).
[21] B. G. Todd, J. Piekarewicz, and P. D. Cottle, Phys. Rev. C **69**, 021301 (2004).
[22] T. Bengtsson and I. Ragnarsson, Nucl. Phys. **A436**, 14 (1985).
[23] J. Zhang, Y. Sun, M. Guidry, L. L. Riedinger, and G. A. Lalazissis, Phys. Rev. C **58**, 2663 (1998).
[24] Y. Sun, J. Zhang, M. Guidry, J. Meng, and S. Im, Phys. Rev. C **58**, 2663 (1998).
[25] N. Tajima and N. Suzuki, Phys. Rev. C **64**, 037301 (2001).
[26] C. Bahri, J. P. Draayer, and S. A. Moszkowski, Phys. Rev. Lett. **68**, 2133 (1992).
[27] K. Rutz, M. Bender, P.-G. Reinhard, J. A. Maruhn, and W. Greiner, Nucl. Phys. **A634**, 67 (1998).
[28] H. Zdunczuk, W. Satula, and R. A. Wyss, Phys. Rev. C **71**, 024305 (2005).
[29] A. Oros, Ph.D. thesis, University of Köln, 1996.

[30] A. Swift and L. R. B. Elton, Phys. Rev. Lett. **17**, 484 (1966).
[31] H. Tyren, S. Kullander, O. Sundberg, R. Ramachandran, P. Isacsson, and T. Berggren, Nucl. Phys. **17**, 321 (1966).
[32] L. Ray and P. E. Hodgson, Phys. Rev. C **20**, 2403 (1979).
[33] V. I. Isakov, K. I. Erokhina, H. Mach, M. Sanchez-Vega, and B. Fogelberg, Eur. Phys. J. A **14**, 29 (2002).
[34] M. Rufa, P.-G. Reinhard, J. A. Maruhn, and W. Greiner, Phys. Rev. C **38**, 390 (1988).
[35] A. L. Blokhin, C. Bahri, and J. P. Draayer, Phys. Rev. Lett. **74**, 4149 (1995).
[36] P. Ring and P. Schuck, *The Nuclear Many-Body Problem* (Springer-Verlag, Heidelberg, 1980).